Challenges and tolerances for a compact and hybrid ultrafast X-ray pulse source based on RF and THz technologies

Journal of Physics: Conference Series **1596** (2020) 012032 doi:10.1088/1742-6596/1596/1/012032

Challenges and tolerances for a compact and hybrid ultrafast X-ray pulse source based on RF and THz technologies

T Vinatier†, R W Assmann, U Dorda, F Lemery, B Marchetti

Deutsches Elektronen Synchrotron, Notkestrasse 85, 22607 Hamburg, Germany

† thomas.vinatier@desy.de

Abstract. We present an in-depth tolerance study and investigation of the main challenges towards the realization of a hybrid compact ultrafast (fs to sub-fs) X-ray pulse source based on the combination of a conventional S-band gun as electron source and a THz-driven dielectric-loaded waveguide as post-acceleration and compression structure. This study allows us determining which bunch properties are the most affected, and in which proportion, for variations of the parameters of all the beamline elements compared to their nominal values. This leads to a definition of tolerances for the misalignments of the elements and the jitter of their parameters, which are compared to the state-of-the-art in terms of alignment precision and stability of operation parameters. The most challenging aspects towards the realization of the proposed source, including THz generation and manufacturing of the dielectric-loaded waveguide, are finally summarized and discussed.

1. Introduction

Particle acceleration beyond the few-MeV level currently requires large infrastructures, of the order of several meters or tens of meters, due to the low operating frequencies (a few GHz) and field amplitudes (a few tens of MV/m in the meter-long structures) of the conventional RF accelerating structures. The same remark holds for the schemes used to compress electron bunches down to durations of the single femtosecond order or below. This is indeed typically done via velocity bunching [1], requiring several meters long accelerating structures and/or drift space, or in magnetic chicanes, which length depends on bunch energy but is typically a few meters.

One of the schemes currently investigated to overcome these limitations, and achieve compact accelerators delivering pC-level ultrashort (fs to sub-fs duration) electron bunches with an energy above the MeV-level, is to use dielectric-loaded structures driven by laser-generated THz[1] pulses [2–5]. In these structures, the frequencies (100 GHz to 10 THz) and field amplitudes (up to a few GV/m) are expected to be much higher than in conventional RF structures. This would allow bunch acceleration and compression by velocity bunching within a few tens of cm, thus reducing the footprint of accelerator beamlines.

One of the first potential applications of THz-driven accelerating structures is to build a compact ultrafast X-ray source based on Inverse Compton Scattering (ICS) [6], delivering fs to sub-fs pulses. However, due to the high frequency, high field amplitude and reduced transverse dimension of THz-driven structures, tolerances to jitters and beamline imperfections are expected to be tight and to represent one of the main challenges towards such compact X-ray sources. In this paper, we present an

[1] In this paper, we consider the THz range of frequency as being between 100 GHz and 10 THz.

in-depth tolerance study (Section 2) and investigation of the main challenges (Section 3) for the realization of a concept of hybrid and compact ultrafast (fs to sub-fs) X-ray pulse source based on ICS previously investigated by the authors [7, 8] within the context of the AXSIS project [9]. The tolerance study aims to define the acceptable margins for several beamline imperfections and various experimental jitters, thus determining which of them are the most challenging to be met.

A schematic layout of the concept of ultrafast X-ray pulse source considered in this paper is shown in Figure 1 (top). The electron source is a conventional laser-driven 1.6 cell S-band RF-gun operating at 2.9985 GHz with its peak field amplitude fixed at 140 MV/m, corresponding to the maximal gradient experimentally achieved with a BNL/SLAC/UCLA gun [10, 11]. A solenoid electromagnet is then used to focus the beam for injection into a THz linac, consisting in a partially dielectric-loaded circular waveguide (DLW) (see Figure 1 bottom) driven by a multicycle THz pulse exciting the TM_{01} mode [12, 13]. In the THz linac, the electron bunch is simultaneously accelerated up to 15-20 MeV and compressed down to duration on the single femtosecond order or below. The beam exiting the THz linac is finally focused by a triplet of quadrupole electro-magnets to the ICS point, where it interacts with an infrared laser to generate X-rays through ICS. More details on the beam dynamics and on the optimization of the layout presented in Figure 1 are available in [7, 8].

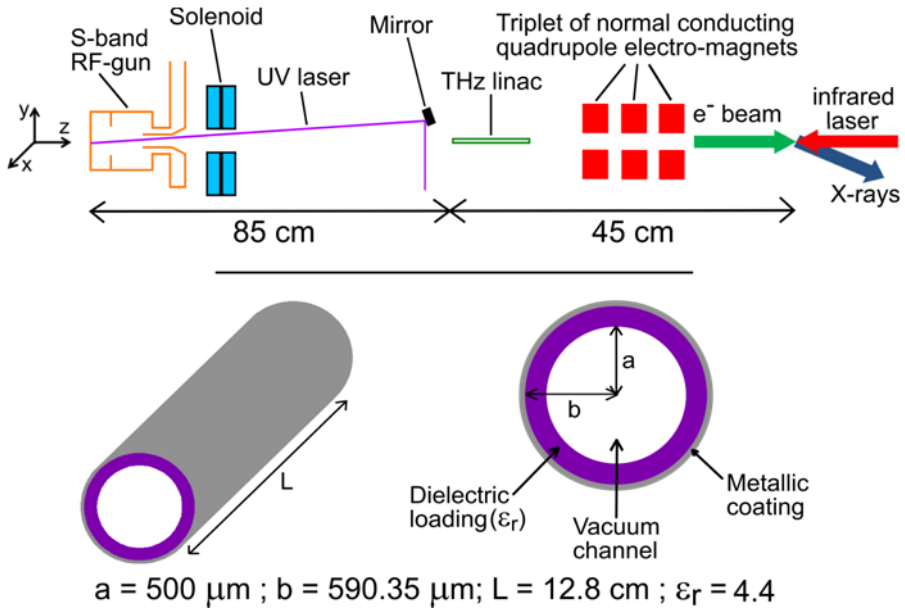

Figure 1. Top: Schematic layout of the ultrafast X-ray pulse source concept. Conditions and parameters: See bulleted list below. Bottom: Schematic of the cylindrical partially dielectric-loaded waveguide intended as THz linac.

As reference case for the tolerance study, we use typical electron bunch properties at the ICS point simulated with ASTRA [14] for a 1 pC charge. They are presented in Table 1, with the following symbols being used throughout the paper to denote the electron bunch properties: Q (charge), $\langle E \rangle$ (average kinetic energy), σ_E (rms energy spread), σ_t (rms length), σ_x-σ_y (rms transverse horizontal-vertical size) and ε_x-ε_y (rms normalized transverse horizontal-vertical emittance). The values in Table 1 are simulated with the following reference beamline parameters:

- Gun region: Peak field E_{mg} = 140 MV/m; UV laser rms duration $\sigma_{t,UV}$ = 75 fs (Gaussian profile) and transverse size $\sigma_{r,UV}$ = 0.5 mm (Gaussian profile cut at 1σ); Solenoid peak field B_0 = 0.258T.
- THz linac: THz pulse central frequency f = 300 GHz; Field amplitude E_{ml} = 115 MV/m.

- Quadrupole triplet: Magnetic length: 5 cm for each quadrupole; Spacing of 8 cm between each quadrupole; Gradients: +9 T/m, -19.5 T/m and +20.5 T/m.

Table 1. Reference electron bunch properties at the ICS point considered in this paper (Q = 1 pC). All the electron bunch properties variations shown in Section 2 are given relative to these ones.

$\langle E \rangle$ (MeV)	σ_E (keV)	σ_t (fs)	σ_x/σ_y (μm)	$\varepsilon_x/\varepsilon_y$ (π.mm.mrad)
17.65	123.2	1.31	10.6/10.5	0.226/0.189

The tolerance study is divided and conducted separately into the four main sections of the layout shown in Figure 1, namely the RF-gun region (RF-gun, UV laser and solenoid), the THz linac, the quadrupole triplet and the ICS interaction region. In this way, the conclusions drawn from the study are not limited to the specific layout shown in Figure 1, but can also be of interest for other applications implying THz-driven DLWs, especially applications relying on injection from a conventional RF-gun into such a DLW.

2. Tolerance study

Different approaches have been used to perform the tolerance study.

For a single and constant beamline imperfection, for example a misalignment, a simple parameter scan has been performed with ASTRA to determine the tolerances. In case jitters of beamline parameters are involved, the relevant quantities to determine the tolerances are the distribution and partition functions of the electron bunch properties at the ICS point under the assumed jitters.

To study a single jitter of a beamline parameter, the procedure is to first run a scan with ASTRA where the parameter is varied step-by-step within a range covering the jitter window. The beam properties at the ICS point are recorded for each step. For each beam properties, the obtained values are then fitted with Matlab to obtain continuous curves over the parameter variation range. Finally, a jitter following a Gaussian distribution with a standard deviation σ_{jit} respective to the parameter nominal value is simulated with Matlab. A large number of values (of the order of 10^6) of the jittering parameter are randomly generated following a Gaussian distribution (with a cut-off at $\pm 3\sigma_{jit}$). For each values, the beam properties are determined using the curves previously obtained with Matlab and recorded. This delivers histograms of the beam properties at the ICS point. Normalizing these histograms, such that their integrals become equal to 1, leads to the distribution functions of the beam properties. An integration of the distribution functions leads to the partition functions of the beam properties.

To study the simultaneous influence of several beamline imperfections and/or parameter jitters, we use the ERROR namelist of ASTRA [14]. This namelist allows running ASTRA for a given number of iterations, while at each iteration a user-defined list of parameters is randomly varied following Gaussian distributions (the standard deviations σ_{jit} of the distributions are user-defined for all the parameters) with a user-defined cut-off ($\pm 3\sigma_{jit}$ in our case). Histograms of the beam properties at the ICS point are obtained in this way, and subsequently their distribution and partition functions are computed as explained above. This method is consuming in terms of computing time. This explains why simpler and faster methods are used when only a single beamline imperfection or parameter jitter is studied.

Throughout Section 2, the relative variation of the electron bunch properties displayed are relative to the reference case shown in Table 1.

A last important point is that the reference case of Table 1 used for the tolerance study is simulated assuming a THz linac with f = 300 GHz. One should note that the higher f, the tighter the tolerances are. Therefore, for cases with f < 300 GHz, the tolerances would be relaxed, by a factor close to the frequency ratio, compared to what is derived in the present section for 300 GHz.

2.1. RF-gun region

For the RF-gun region, from the cathode to the THz linac entrance, the influence of jitters of the following parameters on the electron bunch properties at the ICS point are studied: RF-gun field amplitude, dephasing between the UV laser driving the gun and the RF-field, UV laser pulse energy, UV laser pointing and solenoid peak field.

We first study these jitters altogether, because their combination drives two important jitter sources: the arrival timing jitter and pointing jitter of the electron bunch at the THz linac entrance. Table 2 shows the rms values we assumed for the Gaussian distributions of the jitters in ASTRA. We found σ_E and σ_t to be the most affected properties under the assumed jitters (see Figures 2 (a) and (b)). This was expected since the studied jitters induce a significant bunch arrival timing jitter at the THz linac entrance and thus of the bunch injection phase into it, to which σ_E and σ_t are very sensitive.

Table 2. Rms values assumed for the Gaussian distributions of the jitters simulated with the ERROR namelist of ASTRA.

Gun field amplitude	Gun phase	UV laser pulse energy	UV laser pointing	Solenoid peak field
0.01%	0.006° (≡ 5.5 fs)	3%	35 µm	0.04%

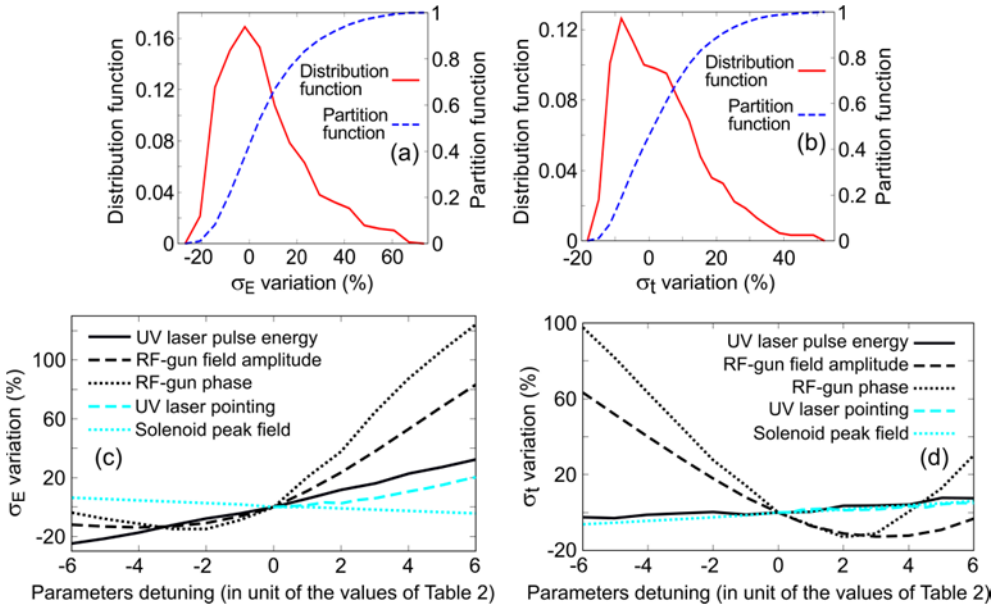

Figure 2. Distribution and partition functions of σ_E (a) and σ_t (b) at the ICS point under the jitters shown in Table 2. Variation of σ_E (c) and σ_t (d) at the ICS point as a function of the detuning of the individual parameters shown in Table 2 compared to their nominal values. The nominal bunch properties are given in Table 1.

The values assumed in Table 2 for the jitters are still not fully satisfactory. In fact, for example, 20% of the shots present a variation of σ_E greater than +25% (see Figure 2 (a)). To determine which of the jittering parameters of Table 2 has the strongest influence, we decoupled them and studied the variation of σ_E and σ_t as a function of the single parameters detuning, expressed in units of the rms values shown in Table 2. This is shown on Figures 2 (c) and (d), which first show that the influence of the parameters detuning is not identical on σ_E and σ_t. Indeed, the strongest variations come for opposite parameters detuning (positive detuning for σ_E and negative detuning for σ_t). For the opposite directions, the variations remain more limited. Figures 2 (c) and (d) then show that, for both σ_E and σ_t,

the strongest influences are from the RF-gun phase and field amplitude jitters. The values assumed in Table 2 for these jitters are at the current state-of-the-art, and even slightly below for the phase [15–19]. To significantly improve the stability of σ_E and σ_t at the ICS point would therefore require improving the RF-gun phase and field amplitude stability beyond the current state-of-the-art and is therefore challenging. Figure 2 (c) also shows that between +1 and +6 units, the contribution of a UV laser pulse energy detuning to the variation of σ_E is around one half (third) of the RF-gun field amplitude (phase) contribution. A small gain could therefore be obtained by reducing its jitter, which is feasible according to the current state-of-the-art of laser intensity stability [20].

2.2. THz linac region

For the THz linac, we first study the field amplitude and phase jitters. The phase jitter represents here only the contribution of the internal phase jitter of the THz pulse source, and does not include the contribution of the electron bunch arrival timing jitter at the THz linac entrance. We then study the influence of THz linac misalignments: translation along x, y and z and rotation around x and y (see Figure 1 for definition).

2.2.1. THz linac field amplitude and phase jitters. Regarding the THz linac field amplitude, our simulations show that a jitter mostly affects $<E>$, σ_E, σ_x and σ_y. A 1% rms jitter would provide a stability of the electron bunch properties already reasonable for operation. In fact, Figure 3 (a) shows that, for the most affected property σ_y, 90% of the shots then exhibit a variation lower than 10%. It also shows that it deteriorates rapidly. Indeed, for a 3% rms jitter, 30% of the shots vary by more than 30%.

Regarding the THz linac phase, a jitter mostly affects $<E>$, σ_E and σ_t. It has to be significantly below 1° rms (≡ 10 fs at 300 GHz) for reasonably stable operation. In fact Figure 3 (b) shows that if this is not the case, for the most affected property σ_E, 20% of the shots will then exhibit a variation greater than +35% and potentially up to +120%. Figure 3 (b) shows that this percentage falls to zero for a jitter below around 0.33° rms (≡ 3 fs at 300 GHz).

A more detailed study on the influence of these two jitters is available in [8].

As explained later in Section 3.1, a promising option to fulfil the requirements in terms of THz pulse power and duration is the laser-based THz generation. The achievable stability for the THz linac field amplitude and phase in this case directly results from the stability of the source laser for the THz pulse driving the THz linac. A 1% rms energy jitter and even below is already achievable as the current state-of-the-art of Joule-class lasers [21], and would be compatible with the tolerances aforementioned. The aspect of the phase stability remains to be investigated.

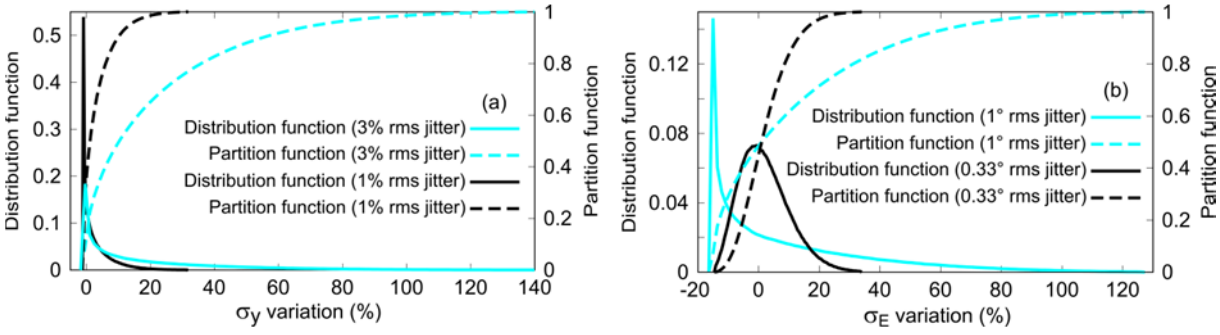

Figure 3. Distribution and partition functions of σ_y (a) and σ_E (b) at the ICS point under jitters of the THz linac field amplitude (a) and phase (b). The nominal bunch properties are given in Table 1.

2.2.2. THz linac misalignments. The THz linac translation respective to its nominal position has been studied up to +/- 0.6 mm along x and y and up to +/- 1 mm along z. Its rotation respective to its nominal position around the x and y axis has been studied up to 9 mrad (≈ 0.52°) with respect to the THz linac entrance and up to 13 mrad (≈ 0.75°) with respect to the THz linac center. Figure 4 shows

the bunch charge as a function of the THz linac misalignments as well as the properties and cases for which the tolerances are the tightest.

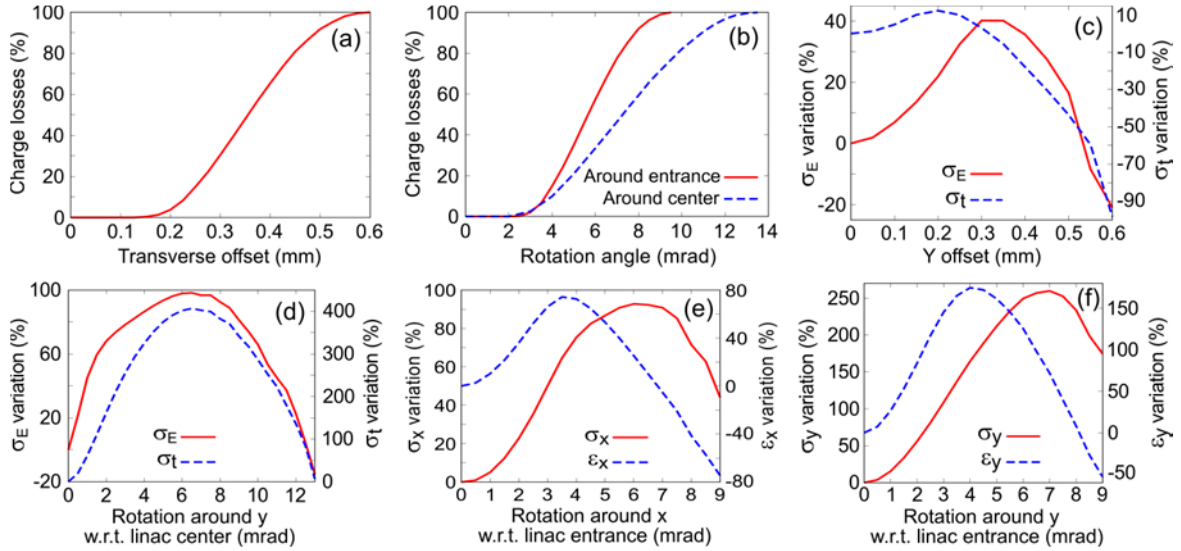

Figure 4. Charge losses as a function of a THz linac transverse offset (a) and rotation (b). Variation of σ_E and σ_t at the ICS point as a function of a THz linac transverse offset along y (c) and rotation around y with respect to its center (d). Variation of σ_x and ε_x (resp. σ_y and ε_y) at the ICS point as a function of a THz linac rotation around x (e) (resp. y (f)) with respect to its entrance. The nominal bunch properties are given in Table 1.

Figures 4 (a) and (b) show that the charge losses start to become significant when the THz linac transverse offset (resp. rotation) exceeds 200 µm (resp. 3 mrad (≈ 0.17°)). A 200 µm transverse offset starts to be reasonable for the electron bunch properties, the most affected (σ_E) varying by +20% (for an offset along y) as shown in Figure 4 (c). Conversely, a 3 mrad THz linac rotation is too big. In fact, as shown in Figures 4 (d), (e) and (f), the variations of σ_E, σ_t, σ_x, ε_x, σ_y and ε_y could then respectively exceed +75%, +250%, +50%, +65%, +100% and +140%. To keep under +20% these variations requires a rotation below 1 mrad (≈ 0.06°) for σ_x, σ_y, ε_x and ε_y, and below 0.5 mrad (≈ 0.03°) for σ_E and σ_t. The asymmetry in the bunch properties variations with THz linac translation (rotation) along (around) x or y, although the THz linac and its field are cylindrically symmetric, comes from the asymmetric transverse focusing provided by the quadrupole triplet downstream.

The 200 µm and 1 mrad (0.5 mrad) tolerances on the THz linac transverse offset and rotation are well within what is achievable with commercially available precision positioning devices like hexapods, which can be on the 10 nm and 1 µrad levels for the absolute position. However, the THz linac alignment will in practice be relative to the other beamline elements. Its practical precision will therefore be ultimately defined by a beam-based alignment procedure, which precision is to be investigated and very likely to be worse than the one of the positioning device.

2.3. Quadrupole triplet region

For the quadrupole triplet, we study the influence of a quadrupole gradients jitter and of quadrupoles misalignments: translations along x, y and z and rotations around x, y and z (see Figure 1 for definition).

2.3.1. Quadrupole gradient jitter. A detuning of the gradients is studied, first independently for the three quadrupoles, in a range of +/- 2% around the nominal gradients. Only the bunch transverse size, especially σ_y, is found to be significantly affected by a quadrupole gradient detuning, especially of the 2nd quadrupole, for the studied range (see Figures 5 (a) and (b)). However, the variations of σ_x and σ_y

become significant only for large quadrupole gradients detuning (typically > 0.5%), much larger than the stability achievable in practice. In fact, commercially available magnet power supplies can deliver a current stability at the 10 ppm level.

Even in the case where the three quadrupoles all have a high uncorrelated 0.5% rms gradient jitter, the variation of σ_x remains below 10% (see Figure 5 (c)) and less than 10% of the shots exhibit for σ_y a variation higher than +20% (see Figure 5 (d)). The quadrupole triplet gradients stability is therefore not expected to represent a challenge for the investigated X-ray pulse source concept.

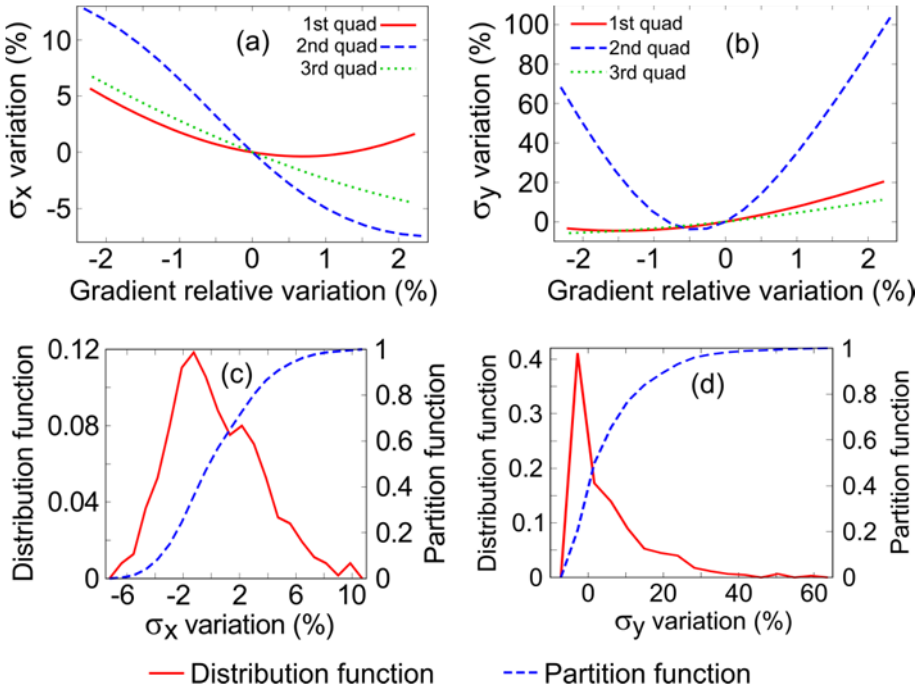

Figure 5. Variation of σ_x (a) and σ_y (b) at the ICS point as a function of the quadrupole gradients variations. Distribution and partition functions of σ_x (c) and σ_y (d) at the ICS point under an uncorrelated 0.5% rms jitter of all the quadrupole gradients. The nominal bunch properties are given in Table 1.

2.3.2. Quadrupole misalignments. The misalignments are studied independently for the three quadrupoles. The translations respective to their nominal positions are studied up to +/- 0.5 mm along x and y and up to +/- 1 mm along z. The rotations respective to their nominal positions are studied up to 20 mrad (≈ 1.15°) around x, y and z. Figure 6 shows the properties and cases for which the tolerances are the tightest.

A translation along y of the 3rd and especially 2nd quadrupole mostly affects σ_E and σ_t (see Figures 6 (a) and (b)) and also, in a less extent, σ_y and ε_y. The asymmetry between the two transverse directions x and y is due to the asymmetric transverse focusing provided by the quadrupole triplet, where the electron bunch is first defocused in the y direction before being strongly focused. With a quadrupoles alignment around or better than 30 µm in the y direction, already demonstrated [22, 23], the variations of σ_E and σ_t would be kept below +8% according to Figures 6 (a) and (b).

The only quadrupole rotation found to have a significant influence on the bunch properties, for the studied range, is the one around z. A rotation around z of the 1st (resp. 2nd) quadrupole especially affects σ_y and ε_y (resp. σ_x and ε_x) as shown in Figures 6 (d) and (c). However, this influence will remain limited in practical conditions. Indeed, even with a rotation of 0.5° (9 mrad), much worse than what is currently achievable with a mechanical alignment, the variations of $\sigma_{x,y}$ and $\varepsilon_{x,y}$ will remain below +20% according to Figures 6 (c) and (d).

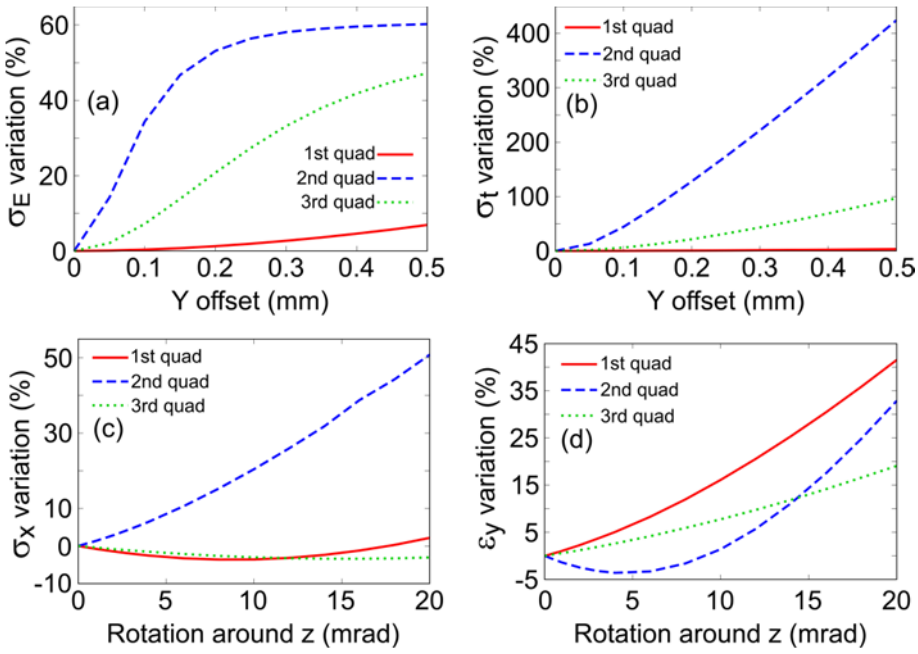

Figure 6. Variation of σ_E (a) and σ_t (b) at the ICS point as a function of quadrupoles translations along y. Variation of σ_x (c) and ε_y (d) at the ICS point as a function of quadrupoles rotations around z. The nominal bunch properties are given in Table 1.

2.4. ICS region

The achievable X-ray pulse properties with the layout shown in Table 1 have been investigated through simulations (see [8] for details), showing its potential tunability between 2.9 and 11.5 keV with, for 400 mJ laser energy, $1.5*10^4$ to $7.7*10^4$ photons/pulse in 1.5% rms bandwidth. In this section, we study the influence of a misalignment between the electron bunch and the laser driving the ICS process both in time and transversely, as well as the influence of a mismatch (without misalignment) between the electron bunch and laser transverse sizes at focus. In addition to the number of photons after collimation $N_{\gamma,\theta coll}$, we use the spectral photon density (SPD), defined as the ratio between the number of photons and their rms bandwidth [24], as the figure of merit to be maximized for the X-ray pulse quality.

$N_{\gamma,\theta coll}$ scales like the inverse of the bunch transverse size squared [24] and the photon pulse bandwidth especially depends, among other contributions, on the bunch transverse size and energy spread [25]. To have a deeper insight into the tolerances for the ICS region, we therefore study four cases corresponding to four different sets of electron bunch properties, with different transverse sizes and energy spreads. Case 1 is the reference shown in Table 1 and Case 2 is the same with the rms transverse size artificially reduced to 6*6 μm^2. These two cases have a relatively large (0.7% rms) energy spread. Case 3 has been simulated with different beamline parameters and has the following properties: $<E>$ = 16.33 MeV, σ_E = 23.8 keV, σ_t = 3.42 fs, σ_x/σ_y = 10.0/9.1 μm and $\varepsilon_x/\varepsilon_y$ = 0.212/0.195 π.mm.mrad, and Case 4 is the same with the rms transverse size artificially reduced to 6*6 μm^2. These two cases have a relatively low (0.15% rms) energy spread (but longer length).

For the laser, we assume a wavelength of 1048 nm, 400 mJ pulse energy, a duration $\sigma_{t,L}$ = 1 ps rms (Gaussian) and a round Gaussian transverse profile with an rms value $\sigma_{r,L}$ fixed to the average of σ_x and σ_y of the electron bunch (except when a transverse size mismatch is considered).

Figures 7 (a) to (f) show the relative variation of $N_{\gamma,\theta coll}$ and SPD for the four cases as a function of the transverse and time offset between the bunch and the laser, and as a function of the transverse size mismatch between them (the laser transverse size being varied). It also shows (Figure 7 (g)) the distribution and partition functions of the bunch transverse offset at the ICS point, coming from a simulation of Case 1 where all the jitters previously mentioned and assumed in the paper are included.

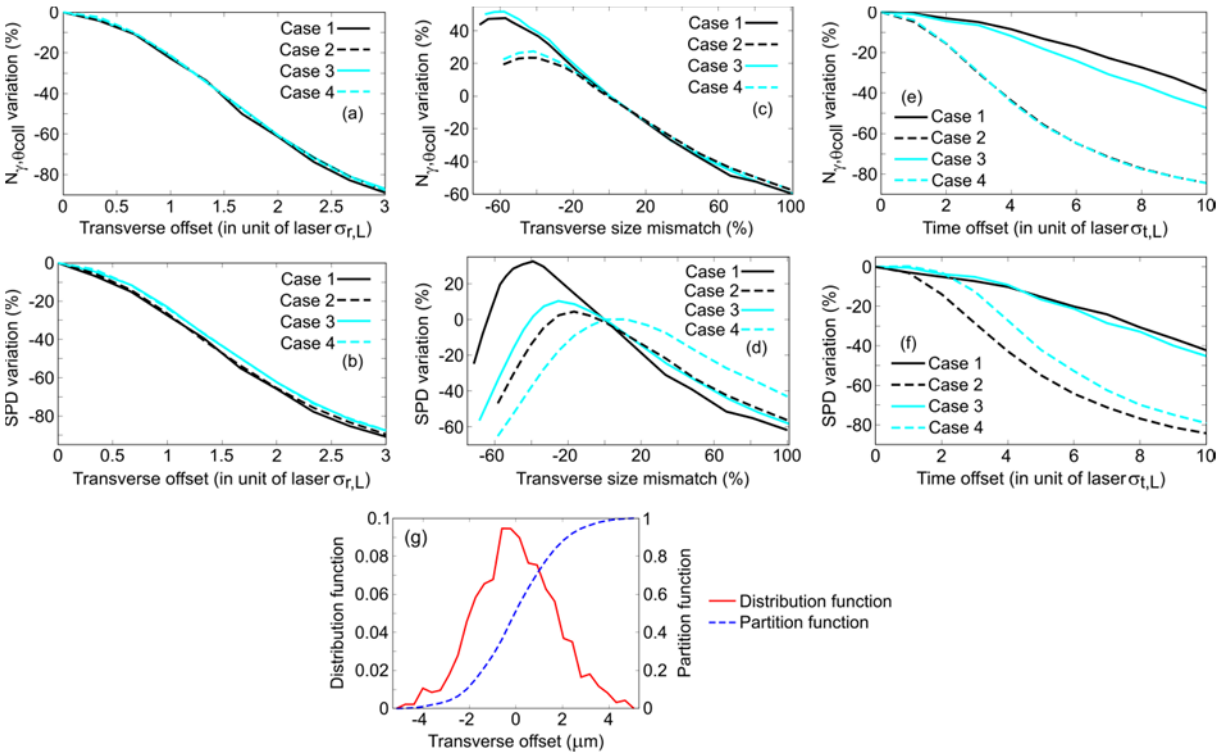

Figure 7. Variation of $N_{\gamma,\theta coll}$ and SPD for four cases (see text for description) as a function of the ICS laser transverse offset (a & b), transverse size mismatch (c & d) and time offset (e & f) respective to the electron bunch. Distribution and partition functions of the electron bunch transverse offset for Case 1 (g) under all the jitters assumed in the paper: RF-gun region: see Table 2; THz linac: 1% (field amplitude) and 1° (phase) rms; Quadrupoles gradients: 0.5% rms.

Figures 7 (a) and (b) show that $N_{\gamma,\theta coll}$ and SPD decrease in a similar way whatever the case, and that the transverse offset between the laser and the bunch should be below 1 unit of $\sigma_{r,L}$ to keep their decrease below -20%. As visible in Figure 7 (g), where Case 1 is considered, this is the case under the jitters assumed in the paper, since the offset is below 5 μm ($0.47\sigma_{r,L}$) for all the shots and the rms value of the distribution function is 1.8 μm ($0.17\sigma_{r,L}$).

Figures 7 (e) and (f) show that the cases with bigger transverse sizes (1 and 3) are the ones having the slower decrease of $N_{\gamma,\theta coll}$ and SPD when the time offset between the laser and the bunch increases. This is due to the decrease of the electron bunch and laser divergences in the vicinity of their focal point when their spot sizes increase. This means that they remain close to their focal sizes in a wider spatial range around their focal points, making $N_{\gamma,\theta coll}$ and SPD less sensitive to the time synchronization between them. For all cases, the time offset is reasonable if it remains below a few units of $\sigma_{t,L}$ (typically 2 times to avoid a decrease of $N_{\gamma,\theta coll}$ and SPD greater than 15%). This means that the synchronization between the bunch and the laser only has to be better than a few ps, which is already demonstrated as achievable (see for example [26]).

Figure 7 (c) shows that for all the cases $N_{\gamma,\theta coll}$ decreases in the same way when the laser becomes larger than the bunch. It is increasing for some time (before decreasing) when the laser becomes smaller than the bunch, but in a different way according to the case. The cases with larger transverse sizes (1 and 3) show a greater increase (up to +45% versus up to +25%) and with the maximum being for a smaller laser size ($\sigma_{r,L}$ reduced by 60% versus by 40%) than the cases with smaller transverse sizes (2 and 4). This is due to the fact that the decrease of the number of electrons interacting with the laser is more compensated for Cases 1 and 3 by the Compton scattering cross-section increase when $\sigma_{r,L}$ decreases than for Cases 2 and 4.

Figure 7 (d) shows that the optimization of $\sigma_{r,L}$ will be the most challenging for Case 1, namely for bunches with large transverse size and energy spread. Indeed, it is for this case that the variations around the SPD maximum are the sharpest. Besides, the SPD maximum is significantly translated compared to the perfect matching since it appears for $\sigma_{r,L}$ reduced by 40%, making it harder to find in practice. For Cases 2 to 4, the optimization of $\sigma_{r,L}$ will be less challenging and important than for Case 1. First, the variations around the SPD maximum are less sharp. Then, the SPD maximum is closer to the perfect matching since the required $\sigma_{r,L}$ variation remains below 20%. Finally, the gain remains limited since the SPD increase between the perfect matching and $\sigma_{r,L}$ maximizing it is below 10%.

3. Other challenges

3.1. THz requirements and generation

Table 3 gathers the THz pulse properties required to achieve the bunch properties shown in Table 1 and also the ones for f = 150 GHz (instead of 300 GHz). For 150 GHz, DLW transverse dimensions twice as big as for 300 GHz have been assumed, namely a = 1 mm and b = 1.1807 mm.

These properties have been calculated using a model starting from the electromagnetic field analytical expression of the TM_{01} mode in the DLW [12, 13]. The value of b required to have a phase velocity v_{ph} equal to c is determined by solving the dispersion relation, arising from the boundary conditions. From the dispersion relation, the dispersion curve (frequency as a function of wavelength) is computed, its derivative at f = 300 GHz (150 GHz) giving access to the group velocity v_g. From v_g, the THz pulse duration required to accelerate the beam over the full DLW length L is calculated. The peak power required to achieve the desired field amplitude is obtained by integration of the complex Poynting vector over a DLW transverse cross-section. Finally, the THz pulse energy is computed by multiplying the peak power by the duration. Detailed information about the equations and procedures used for the derivation of the properties shown in Table 3 are available in [8].

Table 3. Required properties for the THz pulse driving the THz linac, assuming a relative permittivity ε_r = 4.4 for the dielectric layer

f (GHz)	Phase velocity	Group velocity	Duration (ps)	Peak power (MW)	Energy (mJ)
300	c	0.513c	407	23.3	9.5
150	c	0.513c	407	92.7	37.7

Four main methods are currently used to generate fields in the THz range: gyrotrons [27–29], optical rectification of laser pulses in non-linear optical crystals [30–32], CSR/FEL radiation generated in accelerators [33–35] and beam-driven wakefields (for example in dielectric-loaded structures) [36–38]. The methods based on CSR/FEL and beam-driven wakefields require a conventional accelerator with final bunch energy largely above a few MeV, the energy achievable with a conventional RF-gun, and are thus incompatible with a compact X-ray source. However, the beam-driven wakefield is the method coming the closest of the requirements of Table 3, if not fulfilling them, and can thus be useful to perform proof-of-principle experiments. The gyrotrons are currently limited to a few MW peak power, significantly below the requirements, but in long pulses. To use them require to change of approach and not use a travelling wave structure, like the DLW assumed in this paper, but a standing wave structure allowing stocking the THz energy and thus increasing the power (≡ field amplitude) in the structure [39, 40]. Up to recently, the laser-based THz generation was limited far below the requirements. Recent experimental results separately demonstrate the generation of multicycle THz pulses fulfilling (or close to fulfil) the requirements on the duration [32] and on the peak power [41], making laser-based THz generation an appealing candidate for our concept. However, several challenges remain. Especially, the combination of duration and peak power into a single pulse and the field amplitude and phase stability of a laser-generated THz pulse (see Section 2.2.1) are still open questions and require research efforts to be addressed.

3.2. Manufacturing of the dielectric-loaded waveguide

According to Figure 8 (a), the THz pulse phase velocity in the THz linac v_{ph} is very sensitive to a dielectric thickness variation. In fact, keeping the v_{ph} variation below 1‰ require for the DLW manufacturing a dielectric thickness precision better than 150 nm, which is currently not achievable. However, as visible in Figure 8 (b), v_{ph} also depends on the THz pulse frequency f and an error on the dielectric thickness can be compensated by a change of f (typically 2 GHz/µm). It has been demonstrated experimentally that the THz pulse frequency generated by optical rectification of a laser pulse in a non-linear optical crystal is tuneable by changing the crystal temperature (for example with a cryostat), with a rate around 0.3-0.4 GHz/K [42, 43]. The expected error on the DLW dielectric thickness could (and actually would have to) be compensated by adjusting the temperature of the crystal generating the THz pulse. A 1‰ control level on v_{ph} translates into a 1 K control level on the crystal temperature, currently achievable with commercially available cryostats.

Table 4 shows how a 1‰ control level on v_{ph} affects the electron bunch properties by comparing those obtained for $v_{ph} = 0.999c$ and $1.001c$, after adjustment of the solenoid peak field, THz linac phase and quadrupole gradients, with the reference ones for $v_{ph} = c$ (also shown in Table 1). A decrease to $v_{ph} = 0.999c$ comes with an around 50% increase of σ_E and is therefore an issue. However, σ_E is preserved (and even slightly decreased) under an increase to $v_{ph} = 1.001c$. This suggests changing v_{ph} for the reference working point from c (assumed in this paper) to a slightly higher value. It will therefore be interesting for future studies to investigate up to which $v_{ph} > c$ the bunch properties are preserved after proper adjustment of the solenoid peak field, THz linac phase and quadrupole gradients. The objective will be to see if v_{ph} can be sufficiently increased above c to avoid the rapid increase of σ_E observed for $v_{ph} < c$, and also to refine the required level of control on v_{ph}.

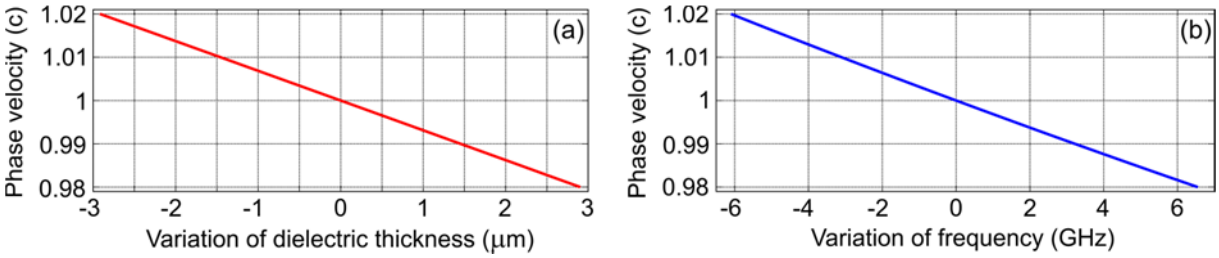

Figure 8. THz pulse phase velocity into the THz linac as a function of the DLW dielectric thickness variation (a) and of the THz pulse central frequency (b). Nominal conditions: $f = 300$ GHz; $\varepsilon_r = 4.4$; $a = 500$ µm; $b - a = 90.35$ µm. Calculations have been made using the analytical model introduced in Section 3.1 (Detailed information on this model are available in [8]).

Table 4. Electron bunch properties at the ICS point ($Q = 1$ pC), obtained after adjustment of the solenoid peak field, THz linac phase and quadrupole gradients, for $v_{ph} = 0.999c$ and $v_{ph} = 1.001c$ compared with the reference ones obtained for $v_{ph} = c$.

v_{ph} (c)	$\langle E \rangle$ (MeV)	σ_E (keV)	σ_t (fs)	σ_x/σ_y (µm)	$\varepsilon_x/\varepsilon_y$ (π.mm.mrad)
0.999	17.65	185.4	1.48	8.3/10.4	0.234/0.185
1	17.65	123.2	1.31	10.6/10.5	0.226/0.189
1.001	17.41	106.8	1.32	8.6/7.4	0.223/0.188

4. Conclusions

We have presented an in-depth tolerance study and investigation of the main challenges towards the realization of a hybrid and compact ultrafast (fs to sub-fs) X-ray pulse source, for which a schematic is shown in Figure 1. These investigations allow defining what the most affected electron bunch

properties at the ICS point are, and in which proportion, for variations of the parameters of all the beamline elements compared to their nominal values.

For the RF-gun region, the stability of the gun parameters (field amplitude and phase) has to be at the current state-of-the-art and even below to be satisfactory, which represents one of the main challenges. On the other hand, the tolerances for the stability of the UV laser energy and pointing and the solenoid peak field are more relaxed and less challenging.

For the THz linac, a field amplitude stability better than 1% rms is necessary, which is challenging but compatible with the current state-of-the-art of the laser pulse energy stability. The question of the THz source phase stability still needs to be investigated, but will surely be one of the main challenges since it has to be significantly better than 1° (≡ 10 fs at 300 GHz). Another potentially challenging aspect is the THz linac alignment. Its translations and rotations compared to the perfect alignment have to be kept respectively below 200 μm and 1 mrad. While this is well within the current absolute precision of positioning devices, the alignment precision will be ultimately determined by the beam-based alignment procedure used to position the THz linac respective to the other beamline elements, and might therefore be worse.

For the quadrupole triplet, all the tolerances in terms of gradient stability and alignment have been found to be compatible with the current state-of-the-art, the tightest one being to keep the second quadrupole offset below 50 μm.

For the ICS interaction region, a synchronization at the few ps level between the electron bunch and the laser, achievable with the current technology, is sufficient. The transverse offset between the bunch and the laser at the interaction point has to be kept below the few μm level. This has been shown achievable in terms of electron bunch pointing jitter at the interaction point under the jitters assumed in this paper for all the beamline elements. The laser transverse size optimization to maximize the SPD is found to become more challenging when the bunch transverse size and energy spread increases, because the laser and electron bunch transverse sizes are then significantly different and the variations around the SPD maximum become sharper.

The requirements in terms of THz pulse properties to drive the THz linac have still not been fulfilled all at once with the current technology. However, recent progress in laser-based THz generation gives optimism that this challenge will soon be solved.

Finally, the very tight precision required for the DLW manufacturing to control the THz pulse phase velocity is an issue. However, a tuning of the THz pulse frequency (achievable by tuning the crystal temperature in laser-based THz generation) would allow compensating the manufacturing errors and retrieve a value close to the desired phase velocity. An important future study will thus be to determine the required control level on the phase velocity, by determining in which range the electron bunch properties can be preserved through a proper adjustment of only the solenoid peak field, THz linac phase and quadrupole gradients.

Acknowledgments

The research leading to these results has received funding from the European Research Council under the European Union's Seventh Framework Programme (FP/2007-2013) ERC Grant Agreement n. 609920, and from Laserlab-Europe (grant agreement n. 654148, European Union's Horizon 2020 research and innovation programme).

References

[1] Anderson S G *et al.* 2005 Velocity bunching of high-brightness electron beams *Phys. Rev. ST Accel. Beams* **8** 014401
[2] Nanni E A, Huang W R, Hong K –H, Ravi K, Fallahi A, Moriena G, Miller R J D and Kärtner F X 2015 Terahertz-driven linear electron acceleration *Nat. Comm.* **6** 8486
[3] Curry E, Fabbri S, Maxson J, Musumeci P and Gover A 2018 Meter-scale Terahertz-driven acceleration of a relativistic beam *Phys. Rev. Lett.* **120** 094801
[4] Hibberd M T *et al.* 2019 Acceleration of relativistic beams using laser-generated terahertz

pulses *Preprint* arxiv:1908.04055
[5] Zhang D, Fakhari M, Cankaya H, Calendron A –L, Matlis N H and Kärtner F X 2020 Cascaded multicycle Terahertz-driven ultrafast electron acceleration and manipulation *Phys. Rev.* X **10** 011067
[6] Blumenthal G R and Gould R J 1970 Bremsstrahlung, synchrotron radiation and Compton scattering of high-energy electrons traversing dilute gases *Rev. Modern Phys.* **42** 237
[7] Vinatier T, Assmann R W, Dorda U, Lemery F and Marchetti B 2018 Simulations on a potential hybrid and compact attosecond X-ray source based on RF and THz technologies *Nucl. Instr. Meth.* A **909** pp 185–92
[8] Vinatier T, Assmann R W, Dorda U, Lemery F and Marchetti B 2019 Simulation of a concept for a compact ultrafast X-ray pulse source based on RF and THz technologies *J. Appl. Phys.* **125** 164901
[9] Kärtner F X *et al.* 2016 AXSIS: Exploring the frontiers in attosecond X-ray science, imaging and spectroscopy *Nucl. Instr. Meth.* A **829** pp 24–9
[10] Palmer D T 1998 The next generation photoinjector *Ph. D. dissertation* (Stanford University)
[11] Dowell D H, Jongewaard E, Limborg-Deprey C, Schmerge J, Li Z, Xiao L, Wang J, Lewandowski J and Vlieks A 2007 Results of the SLAC LCLS gun high power RF tests *Proc. Part. Accel. Conf. 2007 (Albuquerque, New Mexico, USA)* (IEEE) pp 1296–8 TUPMS047
[12] Frankel S 1947 $TM_{0,1}$ mode in circular wave guides with two coaxial dielectrics *J. Appl. Phys.* **18** 650
[13] Chang C T M and Dawson J W 1970 Propagation of electromagnetic waves in a partially dielectric filled circular waveguide *J. Appl. Phys.* **41** 4493
[14] Flöttmann K 2017 *ASTRA manual* DESY Hamburg Germany
[15] Isaev I 2017 Stability and Performances Studies of the PITZ Photoelectron Gun *Ph. D. dissertation* (Hamburg University)
[16] Hoffmann M 2015 Sub-10 fs RF Regulation at REGAE [Powerpoint slides] *Low Level Radio Frequency Workshop 2015 (LLRF15) (Shanghai, China)* Available at https://bib-pubdb1.desy.de/record/292474
[17] Titberidze M, Felber M, Lamb T, Loch R, Sydlo C and Schlarb H 2017 Fs level laser-to-RF synchronization at REGAE *J. Phys. Conf. Ser.* **874** 012085
[18] Schlarb H, Gerth C, Koprek W, Loehl F and Vogel E 2007 Beam based measurements of RF phase and amplitude stability at FLASH *Proceedings 8th European Workshop on Beam Diagnostics and Instrumentation for Particle Accelerators (DIPAC2007) (Venice, Italy)* (Jacow) pp 307–9 WEPC01
[19] Schreiber S 2015 Operation of FLASH [Powerpoint slides] *SPIE Optics + Optoelectronics: Advances in X-ray Free-Electron Laser Instrumentation* (Prague, Czech Republic) Available at https://bib-pubdb1.desy.de/record/208990
[20] Oshima T, Hama Y, Ishikawa H, Kashiwagi S, Kuroda R, Washio M, Yada A, Hayano H and Urakawa J 2001 All-solid-state picosecond laser system for photocathode rf-gun and X-ray generation at Waseda University *Proc. Part. Accel. Conf. 2001 (Chicago, Illinois, USA)* (IEEE) pp 2400–2 WPAH135
[21] Baumgarten C, Pedicone M, Bravo H, Wang H, Yin L, Menoni C S, Rocca J J and Reagan B A 2016 1 J, 0.5 kHz repetition rate picosecond laser *Opt. Lett.* **41** (14) pp 3339–42
[22] Bowden G, Holik P, Wagner S R, Heimlinger G and Settles R 1996 Precision magnet movers for the Final Focus Test Beam *Nucl. Instr. Meth.* A **368** (3) pp 579–92
[23] Krause B, Petrov A, Prenting J, Schloesser M and Sinram K 2008 Precise alignment of magnetic quadrupole axes for PETRA III *IEEE Transactions on Applied Superconductivity* **18** (2) pp 1641–4
[24] Bacci A *et al.* Electron Linac design to drive bright Compton back-scattering gamma-ray

sources *J. Appl. Phys.* **113** 194508
[25] Petrillo V *et al.* 2012 Photon flux and spectrum of γ-rays Compton sources *Nucl. Instr. Meth.* A **693** pp 109–16
[26] Hong K –H *et al.* 2018 Highly-stable, high-power picosecond laser optically synchronized to a UV photocathode laser for an ICS hard x-ray generation *Proc. 9th Int. Part. Accel. Conf. 2018 (Vancouver, Canada)* (Jacow) pp 1504–6 TUPMK008
[27] Flyagin V A, Gaponov A V, Petelin M I and Yulpatov V K 1977 The Gyrotron *IEEE Trans. Microw. Theory Tech.* **25** (6) pp 514–21
[28] Jory H, Blank M, Borchard P, Cahalan P, Cauffman S, Chu T S and Felch K 2003 Test results for a 140 GHz 1 MW gyrotron *AIP Conf. Proc.* **691** pp 224–33
[29] Grimm T L, Kreischer K E and Temkin R J 1993 Experimental study of a megawatt 200-300 GHz gyrotron oscillator *Phys. Fluids B Plasma Phys.* **5** pp 4135–43
[30] Lee Y S, Meade T, Perlin V, Winful H and Norris T B 2000 Generation of narrow-band terahertz radiation via optical rectification of femtosecond pulses in periodically poled lithium niobate *Appl. Phys. Lett.* **76** pp 2505–7
[31] Vodopyanov K L 2006 Optical generation of narrow-band terahertz packets in periodically inverted electro-optic crystals: conversion efficiency and optimal laser pulse format *Opt. Express* **14** pp 2263–76
[32] Jolly S W, Matlis N H, Ahr F, Leroux V, Eichner T, Calendron A –L, Ishizuki H, Taira T, Kärtner F X and Maier A R 2019 Spectral phase control of interfering chirped pulses for high-energy narrowband terahertz generation *Nat. Commun.* **10** 2591
[33] Saldin E L, Schneidmiller E A and Yurkov M V 1997 On the coherent radiation of an electron bunch moving in an arc of a circle *Nucl. Instrum. Meth.* A **398** pp 373–94
[34] Gensch M *et al.* 2014 THz facility at ELBE: A versatile test facility for electron bunch diagnostics on quasi-CW electron beams *Proc. 5th Int. Part. Accel. Conf. 2014 (Dresden, Germany)* (Jacow) pp 933–4 TUZA02
[35] Boonpornprasert P, Krasilnikov M and Stephan F 2017 Calculations for a THz SASE FEL based on the measured electron beam parameters at PITZ *Proc. 38th Int. Free Electron Laser Conf. 2017 (Santa Fe, New Mexico, USA)* (Jacow) pp 411–3 WEP004
[36] Gai W, Schoessow P, Cole B, Konecny R, Norem J, Rosenzweig J and Simpson J 1988 Experimental demonstration of wake-field effects in dielectric structures *Phys. Rev. Lett.* **61** 2756
[37] Antipov S, Babzien M, Jing C, Fedurin M, Gai W, Kanareykin A, Kusche K, Yakimenko V and Zholents A 2013 Subpicosecond bunch train production for a tunable mJ level THz source *Phys. Rev. Lett.* **111** 134802
[38] O' Shea B D *et al.* 2016 Observation of acceleration and deceleration in gigaelectron-volt-per-metre gradient dielectric wakefield accelerators *Nat. Commun.* **7** 12763
[39] Nanni E A, Dolgashev V A, Haase A, Neilson J, Tantawi S, Schaub S C Temkin R J and Spataro B 2017 Prototyping high-gradient mm-wave accelerating structures *J. Phys. Conf. Ser.* **874** 012039
[40] Kutsaev S V *et al.* 2019 Nanosecond rf-power switch for gyrotron-driven millimeter-wave accelerators *Phys. Rev. Applied* **11** 034052
[41] Lemery F, Vinatier T, Mayet F, Assmann R, Baynard E, Demailly J, Dorda U, Lucas B, Pandey A –K and Pittman M 2019 35 megawatt multicycle THz pulses from a homemade periodically poled macrocrystal *Preprint* arxiv:1909.07472
[42] Lee Y S, Meade T, DeCamp M, Norris T B and Galvanauskas A 2000 Temperature dependence of narrow-band terahertz generation from periodically poled lithium niobate *Appl. Phys. Lett.* **77** pp 1244–6
[43] Lee Y S, Meade T, Norris T B and Galvanauskas A 2001 Tunable narrow-band terahertz generation from periodically poled lithium niobate *Appl. Phys. Lett.* **78** pp 3583–5